


Cite this: *RSC Adv.*, 2018, 8, 19690

# Hydrothermal synthesis and characterization of novel yellow pigments based on V<sup>5+</sup> doped BiPO<sub>4</sub> with high near-infrared reflectance†

Cheng Ding, Aijun Han, \* Mingquan Ye, Yu Zhang, Lingyun Yao and Jiling Yang

In this study, a series of novel pigments based on V<sup>5+</sup> doped BiPO<sub>4</sub> have been prepared for the first time via a facile hydrothermal method and characterized using several analytical techniques, such as X-ray diffraction (XRD), field emission scanning electron microscopy (FE-SEM), ultraviolet-visible-near-infrared (UV-vis-NIR) spectrometry, the Commission International de l'Eclairage (CIE) *L\*a\*b\** color scales and thermogravimetry and differential thermal analysis (TG-DTA). The investigation demonstrated that the synthesized pigments of BiP<sub>1-x</sub>V<sub>x</sub>O<sub>4</sub> (*x* = 0.00, 0.01, 0.05, 0.08, 0.10, 0.15) had a monazite-type phase structure and were about 0.25–2 μm in size. Meanwhile, the substitution of V<sup>5+</sup> for P<sup>5+</sup> in BiPO<sub>4</sub> resulted in the band gap of the pigments varying from 3.657 to 3.244 eV and its mechanism was explained by charge-transfer and energy band theory, while the color changed from white to yellow. More importantly, the V<sup>5+</sup> doped pigments possessed high NIR reflectance (>72%) and NIR solar reflectance (≥75.64%) in the range 700–2500 nm. Moreover, coatings colored with synthetic pigments have higher NIR solar reflectance (≥78.59%) than conventional pigments. Additionally, the pigments showed good thermal/chemical stabilities in high-temperature/acid/alkaline tests. In conclusion, the pigments have the potential to be applied as “cool pigments” to reduce energy consumption.

Received 19th March 2018

Accepted 17th May 2018

DOI: 10.1039/c8ra02406e

rsc.li/rsc-advances

## 1. Introduction

The urban heat island phenomenon is increasing, which is mainly due to the replacement of natural vegetation by buildings, causing the temperature of metropolitan centers to rise 10 °C above that in the suburbs.<sup>1</sup> There is no doubt that the phenomenon increases energy consumption, especially the demand for air conditioning in large buildings over past decades. To the best of our knowledge, one of the reasons is that buildings absorb radiant energy in the near-infrared region (NIR: 700–2500 nm) of the solar spectrum, which is precisely the region of heat generation over the entire solar spectrum. Therefore, to mitigate the urban heat island effect by reducing the heat build-up, scientists are looking for new smart materials, like NIR-reflective materials<sup>2,3</sup> which have high NIR solar reflectance, and are usually bright white.<sup>4,5</sup> For example, TiO<sub>2</sub>, an important NIR-reflective material used extensively in energy-efficient buildings because of its high visible (VIS: 400–700 nm) and NIR reflectance (>85%), is currently considered the best pigment among “cool pigments”.<sup>6</sup> However, drawbacks to white pigments are poor esthetics, poor stain resistance, light pollution, *etc.* It is not always possible to cater to consumers'

demands for different colors and functions.<sup>7</sup> Hence, more and more attention is being paid to inorganic pigments that not only possess high NIR reflectance, but also high visible light absorbance.<sup>8</sup>

Rare earth compounds have been proposed as remarkable substitutes for conventional white pigments. For example, Raj *et al.*<sup>9</sup> and Zhang *et al.*<sup>10</sup> synthesized a series of colored inorganic pigments based on terbium-doped yttrium cerate and europium-doped strontium copper silicates and evaluated their color performance and NIR reflectance. Although their properties are good, one problem associated with these inorganic pigments is that their cost is quite high.

Phosphates have already become one of the most researched areas in materials science due to their novel properties.<sup>11,12</sup> BiPO<sub>4</sub> has been widely used as a photocatalyst<sup>13,14</sup> and luminescence material.<sup>15</sup> There are two main crystal structures: the hexagonal and monoclinic forms.<sup>16</sup> Many researchers have reported the microstructures of BiPO<sub>4</sub> and enhanced its optical properties, luminescence properties, and catalytic activity by using various cations as dopants or by complexing with other substances.<sup>17–22</sup> In the recent period, studies have shown that some phosphates have a high NIR reflectance and can obtain various colors *via* doping with different ions. But to our knowledge, few reports have investigated the NIR reflective properties of BiPO<sub>4</sub>. Moreover, BiPO<sub>4</sub> shows advantages of high-temperature chemical stability, oxidation resistance, and relative inexpensiveness compared to rare earth compounds.

School of Chemical Engineering, Nanjing University of Science and Technology, Nanjing 210094, China. E-mail: haj@njust.edu.cn; Tel: +86-25-84438644

† Electronic supplementary information (ESI) available. See DOI: 10.1039/c8ra02406e



In this paper, a series of  $V^{5+}$  doped  $BiPO_4$  pigments exhibiting high NIR reflectance were successfully synthesized by a facile hydrothermal method for the first time. The new yellow pigments, whose formula is  $BiP_{1-x}V_xO_4$  ( $x = 0.00, 0.01, 0.05, 0.08, 0.10, 0.15$ ), were characterized with respect to crystal structure, morphology, chromaticity, and NIR reflective properties. What is more, we tested the NIR reflectance of coatings pigmented with the new synthetic pigments and conventional pigment and then made a comparison. At the same time, the thermal and chemical stability of these pigments were also evaluated in detail.

## 2. Experimental section

### 2.1. Materials

The chemical reagents of bismuth nitrate pentahydrate ( $Bi(NO_3)_3 \cdot 5H_2O$ ), sodium dihydrogen phosphate dihydrate ( $NaH_2PO_4 \cdot 2H_2O$ ), sodium orthovanadate dodecahydrate ( $Na_3VO_4 \cdot 12H_2O$ ) and glycerol ( $C_3H_8O_3$ ) were of high grade (purity > 99%). All of the starting materials were used as received without further purification processes. Distilled water and absolute ethanol ( $C_2H_5OH$ ) were used throughout the whole process.

### 2.2. Process for the preparation of $BiP_{1-x}V_xO_4$ pigments

As a typical experimental process, all the pigments were synthesized by a facile hydrothermal method. According to the formula of  $BiP_{1-x}V_xO_4$  ( $x = 0.00, 0.01, 0.05, 0.08, 0.10, 0.15$ ), stoichiometric proportions of the raw materials were added to 80 mL of glycerol/distilled water mixed-solvent (the volume ratio was 1 : 19) under vigorous magnetic stirring. The amounts of raw materials for synthesis of  $BiP_{1-x}V_xO_4$  samples are listed in Table 1. Subsequently, an ultrasonic cleaner was utilized to dissolve the mixture quickly until the mixture was dispersed more evenly. Finally, the mixture was transferred into a Teflon-lined stainless autoclave and the autoclave was sealed and maintained at 160 °C for 24 h. Then, the reactor was cooled to room temperature in running water. The final product was collected, washed with deionized water and absolute alcohol four times, and then dried at 120 °C for 2 h.

### 2.3. Characterization techniques

The crystalline character and phase purity of the synthesized pigments were characterized by powder X-ray diffraction (XRD)

at room temperature with a Bruker D8 advance diffractometer using Ni-filtered  $Cu K\alpha$  radiation (1.5406 Å). The morphology of the pigments was observed in a field emission scanning electron microscope (HITACHI, S-4800IIFESEM) (FE-SEM) with an acceleration voltage of 15.0 kV. Energy-dispersive X-ray spectroscopy (EDX) as a qualitative and semi-quantitative analysis accessory was used for the elemental analysis or chemical characterization of a sample.<sup>23</sup>

The diffuse reflectance of the samples was measured by an ultraviolet-visible-near-infrared (UV-vis-NIR) spectrophotometer (PerkinElmer Lambda 950 with an integrating sphere attachment), using barium sulfate as the white standard. The NIR solar reflectance ( $R^*$ ) of the pigments and their coatings in the wavelength range from 700 to 2500 nm was calculated in accordance with the American Society of Testing Materials (ASTM) standard number G159-98, as described elsewhere.<sup>24</sup> The function  $R^*$  is given as follows:

$$R^* = \frac{\int_{700}^{2500} r(\lambda) i(\lambda) d(\lambda)}{\int_{700}^{2500} i(\lambda) d(\lambda)} \quad (1)$$

where  $r(\lambda)$  ( $W m^{-2}$ ) is the spectral reflectance experimentally obtained by the UV-vis-NIR spectrophotometer and  $i(\lambda)$  ( $W m^{-2} nm^{-1}$ ) is the solar spectral irradiance obtained from the ASTM standard G159-98. The NIR solar reflectance value was used to quantify the solar radiation, evaluate the reflective performance and qualitatively analyze the effect of cooling energy saving. From the diffuse reflectance ( $R$ ) spectra achieved with the UV-vis-NIR spectrophotometer, the sample absorption edge and the corresponding value of the band gap can be calculated from the Kubelka-Munk (K-M) reemission function, as follows:<sup>25</sup>

$$F(R) = (1 - R^2)/2R \quad (2)$$

The color properties of the pigments were observed by a Konica Minolta (CM-2500d) spectrophotometer with an integrating sphere attachment, and in order to describe the materials' color properties, the color coordinates were established by using the CIE  $L^*a^*b^*$  (1976) method which is recommended by the Commission International de l'Eclairage (CIE).<sup>26</sup> According to the color coordinate system, a positive  $a^*$  value is related to a red color; a negative value, to green. A positive  $b^*$  value is related to a yellow color; a negative value, to blue.<sup>27</sup>  $L^*$  represents the lightness or darkness of the color ( $L^* = 0$  for black and  $L^* = 100$  for white). The color hue noted by the color coordinate  $h^\circ$ , is in the range from 0° to 360° and is defined as  $h^\circ = \tan^{-1}(b^*/a^*)$ .<sup>28</sup> For orange,  $h^\circ$  is in the range of 35–70° and for yellow between 70° and 105°. The parameter  $C^*$  (chroma) expresses the saturation of the color and is defined by using the follow formula:<sup>29</sup>

$$C^* = \sqrt{a^{*2} + b^{*2}} \quad (3)$$

The difference in color between two samples ( $\Delta E^*$ ) could be calculated using this formula:<sup>30</sup>

$$\Delta E^* = \sqrt{(L_2^* - L_1^*)^2 + (a_2^* - a_1^*)^2 + (b_2^* - b_1^*)^2} \quad (4)$$

**Table 1** Amounts of raw materials essential for preparation of  $BiP_{1-x}V_xO_4$  samples

Pigment composition	$Bi(NO_3)_3 \cdot 5H_2O$	$NaH_2PO_4 \cdot 2H_2O$	$Na_3VO_4 \cdot 12H_2O$
$BiPO_4$	2 mmol	2 mmol	0 mmol
$BiP_{0.99}V_{0.01}O_4$	2 mmol	1.98 mmol	0.02 mmol
$BiP_{0.95}V_{0.05}O_4$	2 mmol	1.9 mmol	0.1 mmol
$BiP_{0.92}V_{0.08}O_4$	2 mmol	1.84 mmol	0.16 mmol
$BiP_{0.9}V_{0.1}O_4$	2 mmol	1.8 mmol	0.2 mmol
$BiP_{0.85}V_{0.15}O_4$	2 mmol	1.7 mmol	0.3 mmol



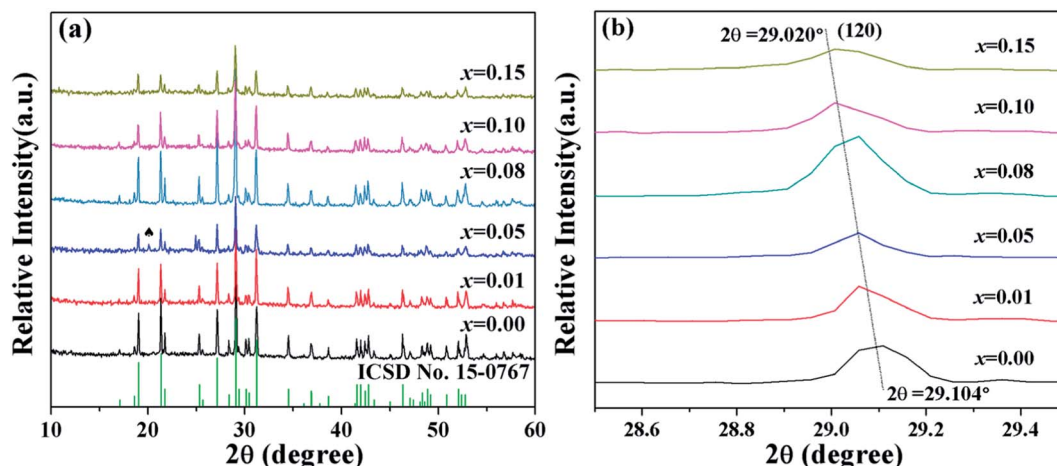


Fig. 1 (a) XRD patterns of  $\text{BiP}_{1-x}\text{V}_x\text{O}_4$  powdered pigments; (b) shift of the Bragg reflections (120) of the doped  $\text{BiP}_{1-x}\text{V}_x\text{O}_4$  pigments.

The thermal property of the pigments was tested by thermogravimetry and differential thermal analysis (TG-DTA) (HENVEN HCT-4). All experiments were carried out in a ceramic crucible with a heating rate of  $5^\circ\text{C min}^{-1}$  from  $25^\circ\text{C}$  to  $1000^\circ\text{C}$  under nitrogen conditions.

### 3. Results and discussion

#### 3.1. Powder XRD analysis

The crystal structure and the phase of pure  $\text{BiPO}_4$  and  $\text{BiPO}_4$  microparticles doped with different contents of vanadium were investigated by XRD. As shown in Fig. 1(a), for undoped  $\text{BiPO}_4$ , all the prominent diffraction peaks in the XRD pattern can be well indexed to the pure monoclinic phase (space group  $P2_1/n$ ) with lattice constants  $a = 6.7526$ ,  $b = 6.9356$ ,  $c = 6.4713$  Å and  $\beta = 103.6966^\circ$ , which is in good agreement with  $\text{BiPO}_4$  (The Inorganic Crystal Structure Database (ICSD) no. 15-0767), indicating the high purity and crystalline of the samples. For instance, the diffraction peaks at  $2\theta = 19.033^\circ$ ,  $21.352^\circ$ ,  $21.757^\circ$ ,  $25.295^\circ$ ,  $27.170^\circ$ ,  $29.104^\circ$ ,  $31.223^\circ$ ,  $34.510^\circ$  correspond to the crystal planes (011), ( $\bar{1}11$ ), (101), (111), (200), (120), (012) of  $\text{BiPO}_4$ . After vanadium-doping, although a negligible hexagonal phase is detected in the sample ( $x = 0.05$ ) at  $2\theta = 20.066^\circ$  (ICSD no. 15-0766), which can be put down to the fluctuation in temperature during the synthesis,<sup>31–34</sup> with an increase in V-dopant concentration in  $\text{BiP}_{1-x}\text{V}_x\text{O}_4$ , on the whole no conspicuous change in the XRD patterns can be observed. Thus, the structure of  $\text{BiP}_{1-x}\text{V}_x\text{O}_4$  was not changed, and the diffraction lines were successfully matched to the monazite-type phase.

For the sake of confirming that  $\text{V}^{5+}$  enters into the lattice structure of  $\text{BiPO}_4$  and forms a solid solution, the evolution of Bragg peaks in the XRD patterns was investigated. Fig. 1(b) describes the shift in the Bragg reflections (120) of the  $\text{BiP}_{1-x}\text{V}_x\text{O}_4$  ( $x = 0.00, 0.01, 0.05, 0.08, 0.10, 0.15$ ) pigments. As shown in Fig. 1(b), it can clearly be seen that the (120) diffraction peaks shift towards a lower diffraction angle as the concentration of  $\text{V}^{5+}$  in the pigments increases (from  $2\theta = 29.104^\circ$  to  $29.020^\circ$ ). We can theoretically understand the shifting effect according to Bragg's law:

$$2d \sin \theta = n\lambda \quad (5)$$

where  $d$  is the inner planar distance,  $\theta$  is the diffraction angle,  $\lambda$  is the diffraction wavelength, and  $n$  is the diffraction series.<sup>35</sup> The above shifting effect of the diffraction peak should be attributed to  $\text{V}^{5+}$  (ionic radius =  $0.355$  Å; coordination number = 4) with larger ionic radius substituting for  $\text{P}^{5+}$  (ionic radius =  $0.170$  Å; coordination number = 4) entering into the  $\text{BiPO}_4$  lattice and causing lattice expansion.<sup>36</sup> Hence, a solid solution of vanadium in the  $\text{BiPO}_4$  lattice is formed in all the prepared pigments.

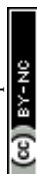
The crystal structure parameters and the cell volume of the  $\text{BiP}_{1-x}\text{V}_x\text{O}_4$  samples were calculated with jade6.0 software. As can be seen in Table 2, the parameters were in the same range for different compositions, and no significant increase was observed, but the inner planar distance of the (120) lattice plane and cell volume came to increase in turn when the content of vanadium increased. This variation is relevant to the difference in ionic radius values of  $\text{P}^{5+}$  and  $\text{V}^{5+}$ . Therefore, it can also demonstrate that vanadium is incorporated into the  $\text{BiPO}_4$  structure.

#### 3.2. Particle size and morphological analysis

The dispersion and grain size of the pigment particles can be detected by SEM. All samples were granular in nature and presented homogeneous grain sizes. The grain sizes were distributed from  $0.25$  to  $2\text{ }\mu\text{m}$ . The surface morphologies of the typical

Table 2 The cell parameters of the  $\text{BiP}_{1-x}\text{V}_x\text{O}_4$  samples

$x$	D-spacing (120) (Å)	$a$ (Å)	$b$ (Å)	$c$ (Å)	$\beta$ ( $^\circ$ )	Volume (Å <sup>3</sup> )
0.00	3.0657	6.7526	6.9356	6.4713	103.6966	294.46
0.01	3.0684	6.7517	6.9358	6.4732	103.7135	294.49
0.05	3.0705	6.7532	6.9362	6.4765	103.7201	294.71
0.08	3.0713	6.7505	6.9436	6.4735	103.6952	294.80
0.10	3.0740	6.7589	6.9297	6.4830	103.7346	294.96
0.15	3.0743	6.7591	6.9351	6.4842	103.7381	295.25



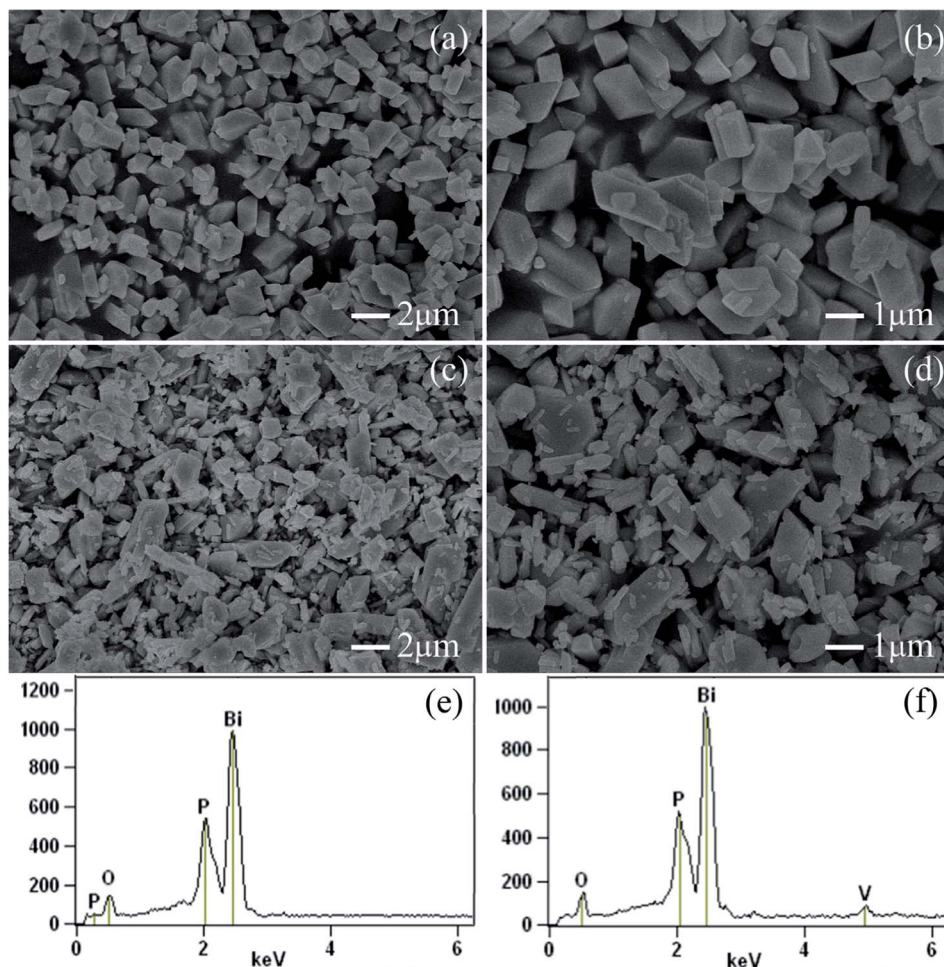


Fig. 2 FE-SEM images of  $\text{BiPO}_4$  ((a) and (b)) and  $\text{BiP}_{0.9}\text{V}_{0.1}\text{O}_4$  ((c) and (d)) powdered pigments. EDX spectra of pure  $\text{BiPO}_4$  (e) and  $\text{BiP}_{0.9}\text{V}_{0.1}\text{O}_4$  (f) pigments.

samples  $\text{BiPO}_4$  and  $\text{BiP}_{0.9}\text{V}_{0.1}\text{O}_4$  are depicted in Fig. 2. For undoped samples, the SEM image shown in Fig. 2(a) displays that the sample is composed of large scales of  $\text{BiPO}_4$  with an irregular prism-shaped structure. Careful observation reveals that the size of the particles typically ranges from 0.5 to 2  $\mu\text{m}$ , as shown in Fig. 2(b). Fig. 2(c) and (d) show the SEM images of  $\text{BiP}_{0.9}\text{V}_{0.1}\text{O}_4$ , which show that the sample consisted of irregular rod-like and prism-shaped particles of microscale magnitude, except for some small nanorods. The micrographs also reveal the presence of agglomeration in the samples. Moreover, all the doped samples had similar morphologies; in other words, the doping of  $\text{V}^{5+}$  does significantly affect the micro-morphology of

the pigments. In addition, there is a tendency for the number of small-sized particles to increase as the doping content increases (some SEM images are shown in the ESI, Fig. S1†). According to K-M theory, the reflectance of materials increases with a decrease in particle size, and the obtained samples contribute to the reflectance of NIR light.

EDX was also used to determine the elemental composition. EDX spectroscopy and the surface elemental composition of the samples are presented in Fig. 2(e) and (f). For pure  $\text{BiPO}_4$ , Fig. 2(e) identifies the presence of all the expected elements. The elemental composition of the doped sample ( $\text{BiP}_{0.9}\text{V}_{0.1}\text{O}_4$ ) was also confirmed by the EDX pattern (as shown in Fig. 2(f)).

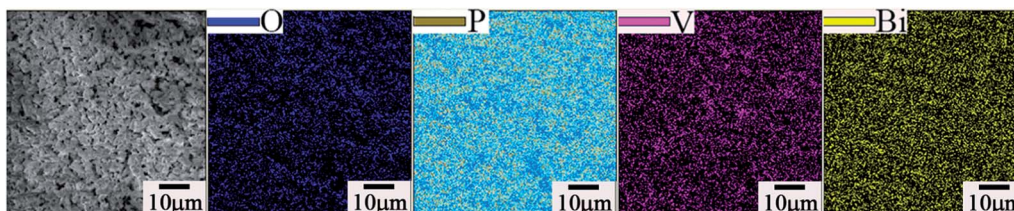


Fig. 3 Elemental mapping of typical  $\text{BiP}_{0.9}\text{V}_{0.1}\text{O}_4$  yellow pigment which confirms that all the elements (O, P, V, Bi) are uniformly distributed in the lattice.



Besides the P, Bi and O peaks, the peak of element V is also observed, which indirectly indicates that ionic vanadium enters into the lattice structure of  $\text{BiPO}_4$  in the final samples. Moreover, in the EDX pattern, the corresponding mass ratios of P and V, are 5.01% and 1.61%, respectively, and these values are close to the expected values (9.11% and 1.67%). Additionally, the elemental mapping analysis of a typical  $\text{BiP}_{0.9}\text{V}_{0.1}\text{O}_4$  yellow pigment is shown in Fig. 3. This mapping shows that all the elements are uniformly distributed in the lattice. This result proves from another viewpoint that vanadium has doped into the lattice of  $\text{BiPO}_4$ .

### 3.3. Diffuse reflectance and chromatic properties analysis

Fig. 4 shows the UV-vis diffuse reflectance curve of the  $\text{BiP}_{1-x}\text{V}_x\text{O}_4$  ( $x = 0.00, 0.01, 0.05, 0.08, 0.10, 0.15$ ) powdered samples. As can be seen from the spectra,  $\text{BiPO}_4$  is almost totally reflective in the visible spectral region, and thus the color of  $\text{BiPO}_4$  presents as white. The UV-vis diffuse reflectance spectrum of  $\text{BiPO}_4$  mainly originates from indirect transitions. Compared with pure  $\text{BiPO}_4$ , although the reflectivity of the doped samples in the UV-vis region is reduced, a chromatic color is given (as shown in Fig. 5). In addition, in the 525 to 700 nm waveband, the reflectivity appears to show an increasing trend as the doping amount increases. It is clearly shown that a moderate increase in doping amount is helpful to improve the reflectivity.

We usually use the K-M reemission function, which is used as a measurement of absorption *via* powder, to convert the reflectance spectrum to the corresponding absorption spectrum. As shown in Fig. 6, a curve of K-M and wavelength is drawn and the absorption edge is decided from the curve. With the increase in doped  $\text{V}^{5+}$ , the absorption edge changes from 338 to 381 nm. It should be noted that only the material absorbs visible light, showing color; otherwise it is white or colorless. The absorption edge of  $\text{BiPO}_4$  occurs at about 338 nm, and it is almost completely reflective in the visible spectral region, so it is white. However, the absorption edge of the doped samples is mainly concentrated in the range of violet light (purple corresponding to the wavelength range of 350–455 nm), thus the color of the samples is yellow according to the principle of complementary colors (see Fig. 4 and 5). The energy band gap

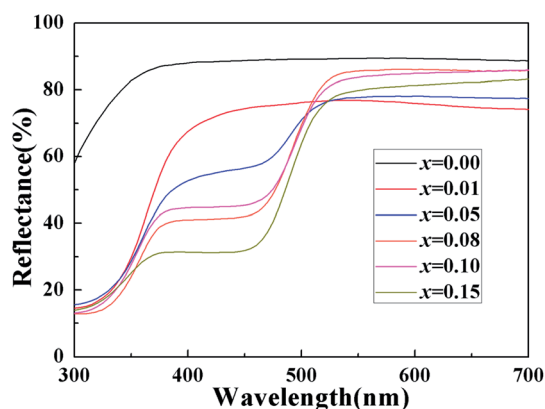


Fig. 4 UV-vis diffuse reflectance spectrum of  $\text{BiP}_{1-x}\text{V}_x\text{O}_4$  powdered pigments.

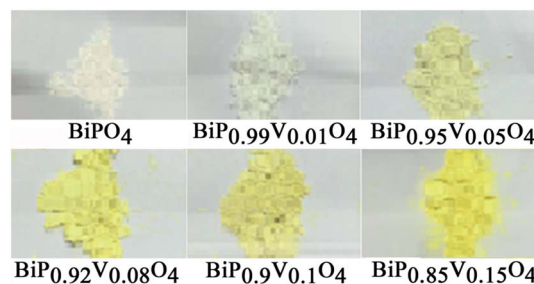


Fig. 5 Photographs of pigments of the  $\text{BiP}_{1-x}\text{V}_x\text{O}_4$  system.

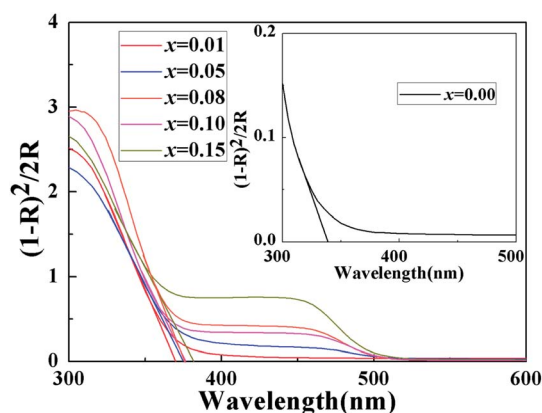


Fig. 6 Absorption edge of  $\text{BiP}_{1-x}\text{V}_x\text{O}_4$  powdered samples measured with K-M theory.

can be also obtained by using the K-M reemission function. And the value of the wavelength is replaced in the formula  $E$  (eV) =  $1236/\text{wavelength (nm)}$ . To be more specific, the energy coordinates of the dot on the low-energy side of the plot where the linear increase in the function  $[(F(R)h\nu)^2]$  starts have been deemed to be the value of the band gap energy of the semi-conductors.<sup>37</sup> As shown in Fig. 7, the band gap of the pigments varies over the range from 3.657 to 3.244 eV as the incorporation of  $\text{V}^{5+}$  increases, so the color of the samples changes from white to yellow. The band gap of the samples is shown in Table 3. These results clearly confirm that the electronic structures of the  $\text{BiP}_{1-x}\text{V}_x\text{O}_4$  samples with different doping content are slightly different.

The introduction of vanadium caused a decrease in the band gap and the bathochromic shift of the absorption line can be assigned to the following reasons: (1) the incorporation of vanadium replaces phosphorus and produces vanadium oxy tetrahedra; therefore, one of the reasons could be attributed to the charge-transfer transitions of the  $[\text{VO}_4]^{3-}$  group; (2) for pure  $\text{BiPO}_4$ , the conduction band minimum (CBM) and valence band maximum (VBM) consist of the bismuth 6p orbitals with a small contribution from the oxygen 2p orbitals and the oxygen 2p orbitals with a small contribution from the bismuth 6s orbitals, respectively.<sup>32</sup> However, the doping samples have transitioned from the hybrid orbital of the bismuth 6s orbitals and oxygen 2p orbitals to the 3d orbitals of vanadium. That is, another reason is the doping with  $\text{V}^{5+}$  cations, resulting in an N-type



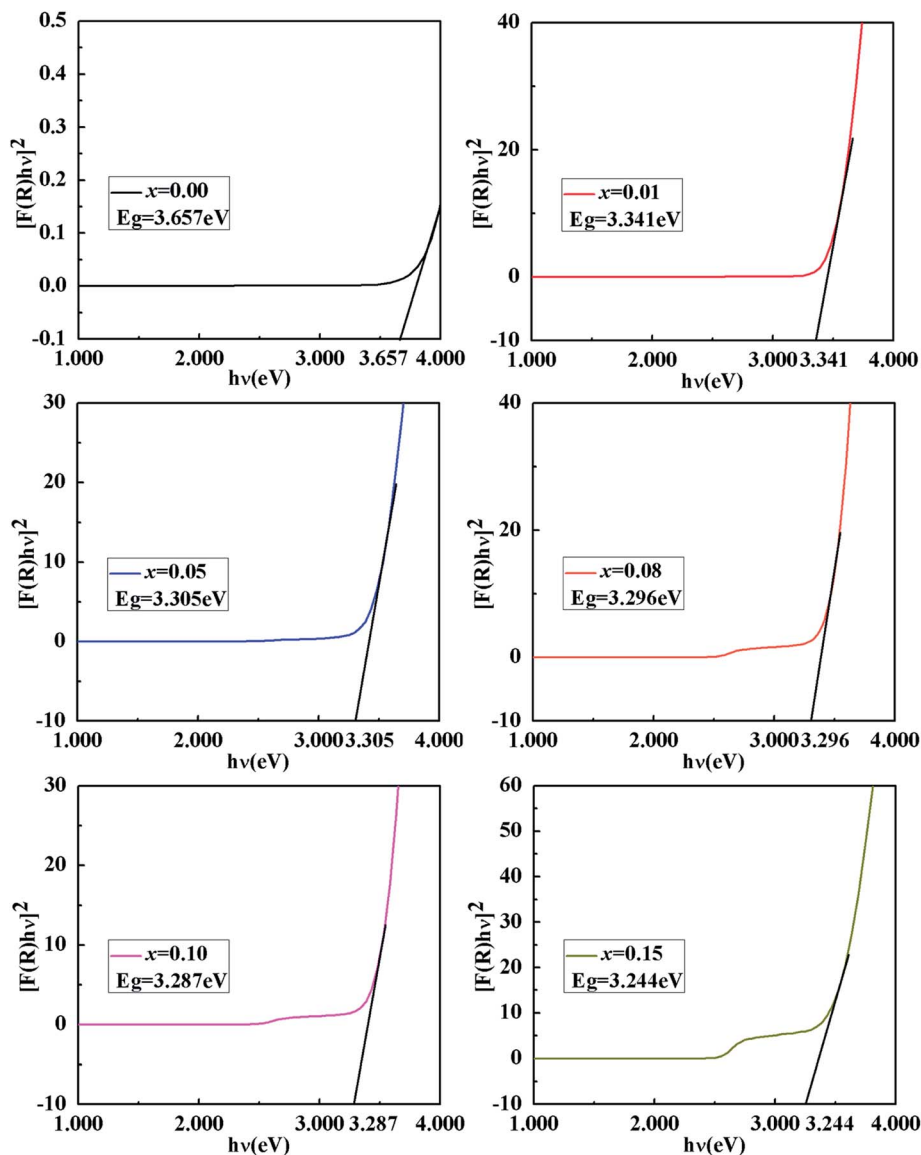


Fig. 7 K–M transformed reflectance spectra of  $\text{BiP}_{1-x}\text{V}_x\text{O}_4$  powdered samples.

semiconductor being formed and the bottom of the conduction band decreasing. The schematic band structures of  $\text{BiPO}_4$  and vanadium ion substituted  $\text{BiPO}_4$  are shown in Fig. 8. Thus, the energy band gap of the charge-transfer transition gradually decreased during the vanadium-doping process.

The CIE chromaticity diagram of  $\text{BiP}_{1-x}\text{V}_x\text{O}_4$  ( $x = 0.00, 0.01, 0.05, 0.08, 0.10, 0.15$ ) powdered samples is shown in Fig. 9. The CIE chromaticity coordinates ( $x, y$ ) are deduced on the basis of the following equations<sup>38</sup> and the coordinate values are summarized in Table 3.

Table 3 Color coordinates, absorption edges and band gaps of  $\text{BiP}_{1-x}\text{V}_x\text{O}_4$  pigments

$x$	CIE( $x, y$ )	Color coordinates					Absorption edges (nm)	Band gaps (eV)
		$L^*$	$a^*$	$b^*$	$c^*$	$h^\circ$		
0.00	(0.3145, 0.3323)	96.85	−0.27	0.64	0.70	112.90	338	3.657
0.01	(0.3150, 0.3331)	97.78	−0.48	1.09	1.20	113.77	370	3.341
0.05	(0.3369, 0.3630)	93.59	−3.35	15.77	16.13	102.00	374	3.305
0.08	(0.3605, 0.3894)	92.99	−3.20	29.89	30.07	96.11	375	3.296
0.10	(0.3564, 0.3845)	91.33	−3.51	27.15	27.37	97.36	376	3.287
0.15	(0.3714, 0.4051)	89.74	−5.80	36.31	36.77	99.07	381	3.244



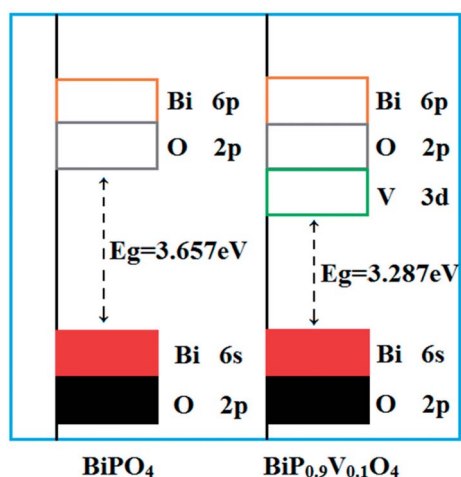


Fig. 8 Band structure models of  $\text{BiPO}_4$  and  $\text{BiP}_{0.9}\text{V}_{0.1}\text{O}_4$ .

$$x = \frac{x}{x + y + z} \quad (6)$$

$$y = \frac{y}{x + y + z} \quad (7)$$

As can be seen from Fig. 9, the chromatic coordinates of  $\text{BiPO}_4$  and  $\text{BiP}_{0.99}\text{V}_{0.01}\text{O}_4$  are near the Standard Source C (illuminant C (0.3101, 0.3162)), and the color of the other samples gets gradually closer to the yellow area as the doping content increases from 0.05 to 0.15, which corresponds with the fact that the color of the samples varies from white to yellow (as shown in Fig. 5), which can be attributed to the substitution of  $\text{V}^{5+}$  for  $\text{P}^{5+}$  in the  $\text{BiPO}_4$  crystal lattice, causing the absorption

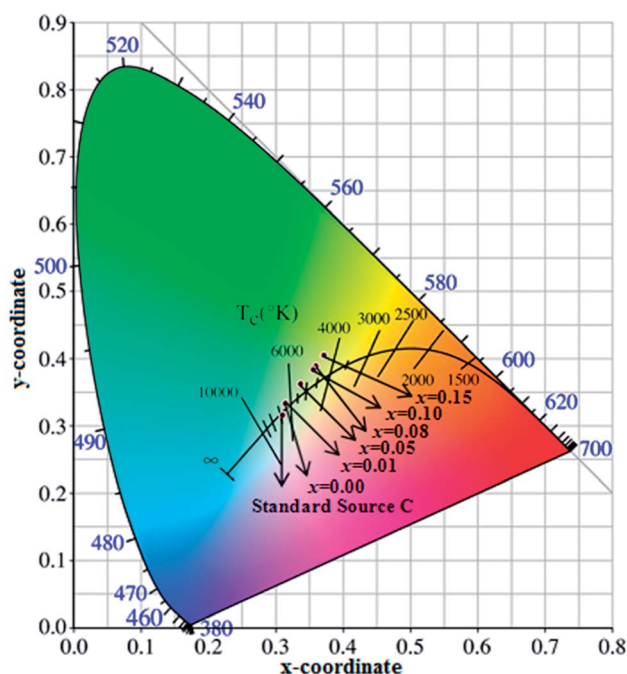


Fig. 9 Chromaticity coordinates of  $\text{BiP}_{1-x}\text{V}_x\text{O}_4$  powdered pigments compared to the 1931CIE Standard Source C.

edge of the pigment samples to shift to longer wavelength (338 to 381 nm). In addition, the color temperature marks the different spectral components that pigments contain. As shown in Fig. 9, the spectral components of the samples are mainly concentrated in the yellow part.

The chromatic properties of  $\text{BiP}_{1-x}\text{V}_x\text{O}_4$  ( $x = 0.00, 0.01, 0.05, 0.08, 0.10, 0.15$ ) powdered pigments were evaluated by CIE 1976  $L^*a^*b^*$  color coordinates, which are listed in Table 3. On the one hand, the progressive doping of  $\text{V}^{5+}$  into  $\text{BiPO}_4$  results in a continuous increase in the yellow component ( $b^*$  increases from 0.64 to 36.31) and chroma ( $C^*$  increases from 0.70 to 36.77) values of the pigments. On the other hand, the substitution of  $\text{V}^{5+}$  for  $\text{P}^{5+}$  in  $\text{BiPO}_4$  brings about a small decrease in the green component ( $a^*$  decreases from  $-0.27$  to  $-5.80$ ). As a result, the color of the pigments changes from white to yellow. Meanwhile, the changes in color result in a decrease of lightness ( $L^*$ ) from 96.85 to 89.74, which shows that the samples become darker, but this is still higher than the value found by Sandhya Kumari *et al.*<sup>39</sup> who prepared P substituted  $\text{BiVO}_4$  pigments ( $L^*$  around 77). Moreover, doping does not have a prominent effect on the hue angle ( $h^\circ$ ). The hue angles ( $h^\circ$ ) of vanadium doped  $\text{BiPO}_4$  pigments (from  $x = 0.05$  to  $x = 0.15$ ) were found to be in the yellow area about the cylindrical color space ( $h^\circ = 70\text{--}105$  for yellow). In a word, these results make this pigment a potential candidate for an environmental yellow pigment.

### 3.4. NIR reflectance analysis of the powdered pigments

Solar radiation is composed of 5% UV radiation, 43% VIS radiation and 52% NIR radiation. Pigments have colors due to absorbing a lot of visible radiation and reflecting little radiation. Therefore, we concentrate on their NIR reflectance, and the main NIR radiation region ranging from 700 to 1400 nm, within which most solar energy lies.<sup>40</sup> The NIR reflectance spectra of the powdered samples  $\text{BiP}_{1-x}\text{V}_x\text{O}_4$  ( $x = 0.00, 0.01, 0.05, 0.08, 0.10, 0.15$ ) and a conventional pigment with a similar color, were recorded in the range from 700 to 2500 nm using barium sulfate as a reference, as exemplified in Fig. 10(a). The result according to Fig. 10(a) illustrates that the  $\text{V}^{5+}$  doped pigment possesses a high NIR reflectance ( $>72\%$ ) in the range 700–2500 nm with a yellow color and the reflectance of white  $\text{BiPO}_4$  is more than 80% throughout the NIR spectrum. Among these, when the doping concentration is between 0.08 and 0.15, the NIR reflectance is as high as about 90% and has higher brightness ( $L^* > 89$ ) than the P substituted  $\text{BiVO}_4$  pigments prepared by Sandhya Kumari *et al.* ( $L^*$  around 77).<sup>39</sup> At the same time, compared with the currently commercially available nickel antimony titanium yellow rutile pigments ( $\text{TiNiY}$ ), the pigments we have prepared possess a higher NIR reflectance while having similar colors (the  $\text{TiNiY}$  NIR reflectance is about 72%).<sup>41</sup> It is worth noting that we have determined the optimal doping amount to be about 0.1. It can be seen from Fig. 10(a) that when the doping amount reaches 0.1, the reflectivity is the highest. More importantly, the NIR reflectance of the synthesized yellow pigments is higher than that of conventional pigment. Moreover, the NIR reflectance of the  $\text{BiP}_{0.9}\text{V}_{0.1}\text{O}_4$  is



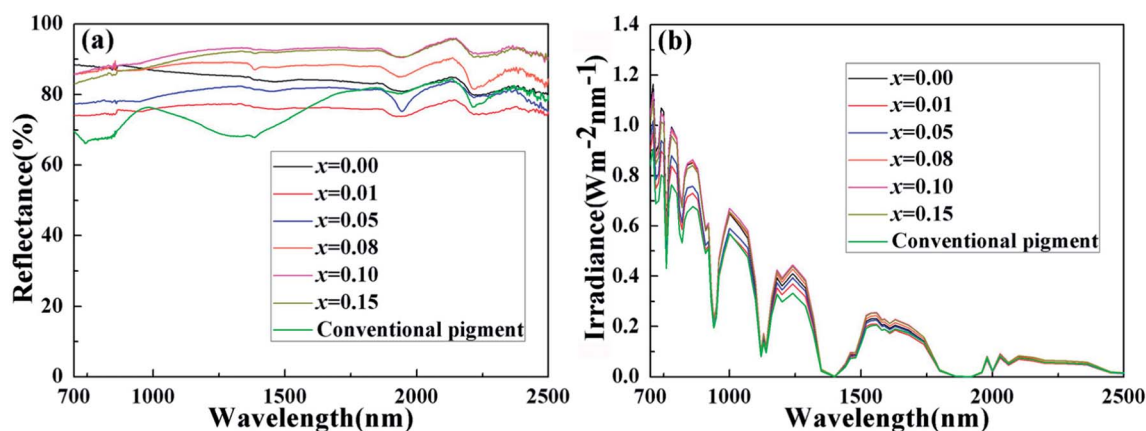


Fig. 10 (a) NIR reflectance and (b) solar radiation energy distribution of  $\text{BiP}_{1-x}\text{V}_x\text{O}_4$  powdered pigments.

Table 4 The values of NIR solar reflectance of powdered samples

Pigment composition	NIR solar reflectance
Conventional pigment	72.43%
$\text{BiPO}_4$	86.40%
$\text{BiP}_{0.99}\text{V}_{0.01}\text{O}_4$	75.64%
$\text{BiP}_{0.95}\text{V}_{0.05}\text{O}_4$	79.61%
$\text{BiP}_{0.92}\text{V}_{0.08}\text{O}_4$	87.61%
$\text{BiP}_{0.9}\text{V}_{0.1}\text{O}_4$	90.16%
$\text{BiP}_{0.85}\text{V}_{0.15}\text{O}_4$	88.52%

over 15% higher than that of conventional pigment in the range 700–1500 nm. Some reports indicated that the changes in reflectance of materials can be caused by a combination of various factors, such as electronic structure, particle size, particle size distribution, phase structure, chemical composition, particle morphology and smoothness, density, *etc.*<sup>39,42</sup>

Fig. 10(b) exemplifies the solar radiation energy distribution of the  $\text{BiP}_{1-x}\text{V}_x\text{O}_4$  system. This clearly confirms that the energy distribution of solar radiation mainly lies in the shortwave range. Table 4 shows the NIR solar reflectance of the samples and of conventional yellow pigment calculated according to

ASTM standard number G159-98. It can be clearly seen from Table 4 that the NIR solar reflectance of conventional yellow pigment ( $R^* = 72.43\%$ ) is lower than that of all vanadium-doped  $\text{BiPO}_4$  samples ( $R^* \geq 75.64\%$ ). The NIR solar reflectance of the synthesized pigments evidently increases from 75.64% to 90.16% (from  $x = 0.01$  to  $x = 0.15$ ). Thus, the  $\text{BiP}_{1-x}\text{V}_x\text{O}_4$  ( $x = 0.00, 0.01, 0.05, 0.08, 0.10, 0.15$ ) pigments have potential as “cool pigments” with energy saving performance due to their comparatively high solar reflectance.

### 3.5. NIR solar reflectance analysis of the pigmented coatings

To keep indoors cool in a hot summer, energy saving materials with high solar reflectance are in great demand, especially for nonwhite materials that absorb less NIR radiation. In order to evaluate the performance of the materials as “cool pigments” for cutting down heat build-up, we painted the synthetic pigments onto an aluminum sheet substrate. The preparation method was as follows:<sup>43</sup> Firstly, the synthesized pigments or conventional yellow pigment and alkyd resin with a mass ratio of 1 : 1 were mixed uniformly. Secondly, the homogeneous mixture was painted onto the aluminum sheet substrate (20 mm × 20 mm × 3 mm) and dried in air for about seven days. Fig. 11

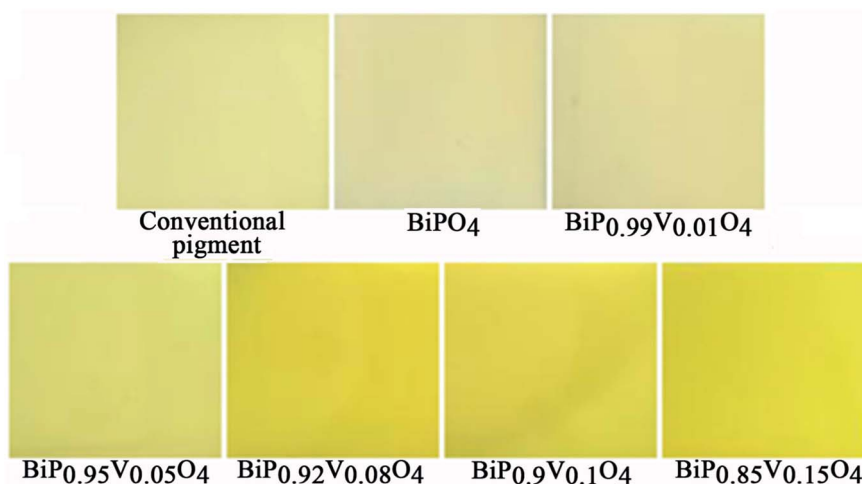


Fig. 11 Photographs of pigments coated onto the aluminum sheet substrate.



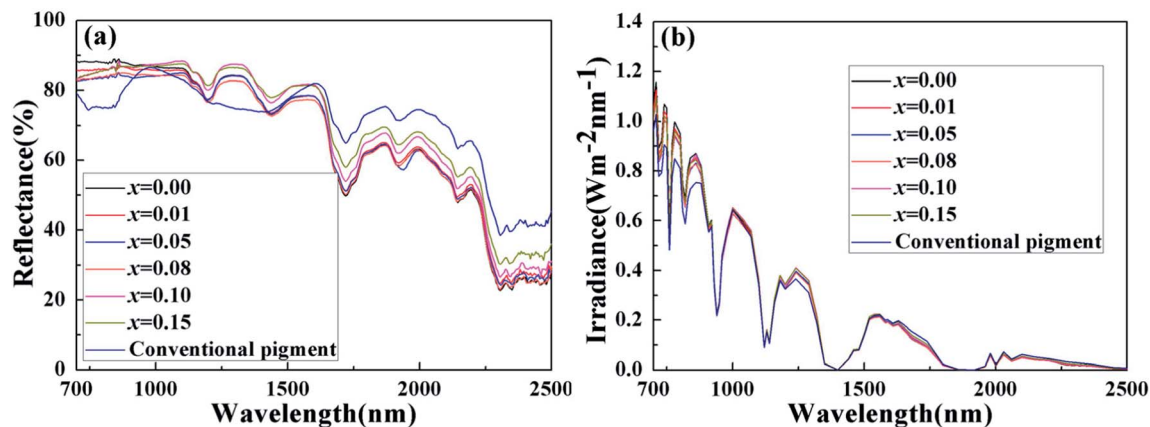


Fig. 12 (a) NIR reflectance and (b) solar radiation energy distribution of the pigmented coatings.

**Table 5** The detailed values of NIR solar reflectance of the pigmented coatings

Pigment composition	NIR solar reflectance
Conventional pigment	77.40%
BiPO <sub>4</sub>	81.09%
BiP <sub>0.99</sub> V <sub>0.01</sub> O <sub>4</sub>	80.24%
BiP <sub>0.95</sub> V <sub>0.05</sub> O <sub>4</sub>	78.80%
BiP <sub>0.92</sub> V <sub>0.08</sub> O <sub>4</sub>	78.59%
BiP <sub>0.9</sub> V <sub>0.1</sub> O <sub>4</sub>	81.50%
BiP <sub>0.85</sub> V <sub>0.15</sub> O <sub>4</sub>	81.74%

presents photographs of the pigmented coatings. Finally, the NIR reflectance of these coatings was assessed with a UV-vis-NIR spectrophotometer.

Fig. 12(a) and (b) show the NIR reflectance spectra and the corresponding solar radiation energy distribution of the pigmented coatings, respectively. The curves clearly illustrate that the conventional coating has a lower NIR reflectance than the BiP<sub>1-x</sub>V<sub>x</sub>O<sub>4</sub> system coatings in the 700–1500 nm region (as shown in Fig. 12(a)). And the NIR solar reflectance values of the pigmented coatings are shown in Table 5. Therefore, although the NIR reflectance of the conventional coating is higher than

the BiP<sub>1-x</sub>V<sub>x</sub>O<sub>4</sub> system pigmented coatings between 1500 nm and 2500 nm, the total NIR solar reflectance is still lower than that of the pigmented coatings we prepared. All of these results indicate that the doped samples we synthesized could be used as potential cool materials, reducing energy consumption for cooling in future.

### 3.6. Thermal and chemical stability analysis

To investigate the thermal performance of the powdered pigments, TG–DTA plots of the typical synthesized pigments BiPO<sub>4</sub> and BiP<sub>0.9</sub>V<sub>0.1</sub>O<sub>4</sub> are depicted in Fig. 13. The thermal behaviour of the samples was followed from room temperature to 1000 °C. The TG curves clearly illustrate that even if the temperature is as high as 1000 °C the pigments undergo no variation in mass. Moreover, the DTA profile indicates no exothermic or endothermic effect whatsoever, which suggests the absence of any physico-chemical transformation in the investigated temperature interval. These results show that the pigments have good thermal stability.

Chemical stability is very crucial to the performance of pigments. And in order to evaluate the chemical stability of the typical synthesized samples, the water and acid/alkali resistance of the typical pigment BiP<sub>0.9</sub>V<sub>0.1</sub>O<sub>4</sub>, was investigated using 10% H<sub>2</sub>SO<sub>4</sub>, 10% HNO<sub>3</sub>, 10% NaOH solution and H<sub>2</sub>O, respectively.

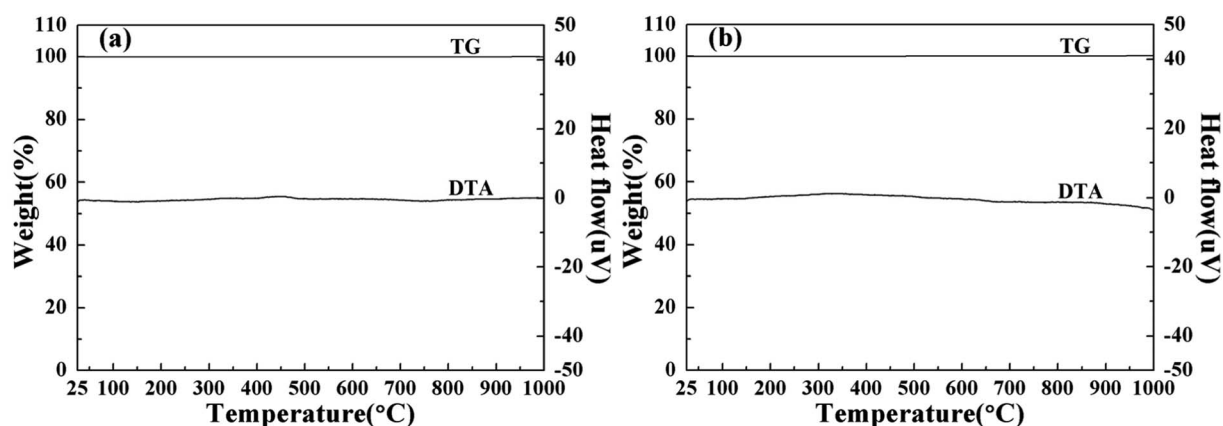


Fig. 13 TG–DTA curves of (a) BiPO<sub>4</sub> and (b) BiP<sub>0.9</sub>V<sub>0.1</sub>O<sub>4</sub> powdered samples.



Table 6 The color coordinates of the treated  $\text{Bi}_{0.9}\text{V}_{0.1}\text{O}_4$  pigments

No.	$L^*$	$a^*$	$b^*$	$\Delta E^*$
In air	91.33	−3.51	27.15	—
$\text{H}_2\text{O}$	91.45	−3.37	26.94	0.28
$\text{NaOH}$	90.91	−4.12	29.28	1.98
$\text{H}_2\text{SO}_4$	90.40	−3.75	26.90	0.99
$\text{HNO}_3$	90.61	−3.21	26.77	0.87

And the concentration of the solution was five times higher than that of the standard (GB/T 5211.5-2008). A pre-weighed quantity of a typical pigment was treated with water, acid/alkali and soaked for ten minutes with constant stirring *via* a magnetic stirrer. Then the powdered sample was filtered, washed with deionized water several times, dried and weighed again. The results indicated that the weight loss of the pigment sample can be ignored after testing in acid, alkali and water. Table 6 shows the color coordinates of the pigment after the water, acid and alkali treatment. For industrial application of inorganic pigments, high color durability ( $\Delta E^*$  values less than 2 or 3) is required.<sup>44</sup> Compared with the untreated sample, the small values of  $\Delta E^*$  confirm that the chemical stability of the pigment is better. They also indicated that the water and acid resistances of the samples are very good.

## 4. Conclusions

In this paper, we have employed a facile hydrothermal method to synthesize a series of inorganic pigments  $\text{Bi}_{1-x}\text{V}_x\text{O}_4$  ( $x = 0.00, 0.01, 0.05, 0.08, 0.10, 0.15$ ) for the first time, which display a range of colors from white to yellow, which can be attributed to the substitution of  $\text{V}^{5+}$  for  $\text{P}^{5+}$  in the  $\text{BiPO}_4$  crystal lattice, causing the absorption edge of the pigment samples to shift to longer wavelength (338 to 381 nm). The doped samples are similar in morphology and their sizes are in the range of 0.25 to 2  $\mu\text{m}$ . More importantly, these pigments exhibited high NIR reflectance (>72%) in the range 700–2500 nm, and possessed higher NIR solar reflectance than a conventional pigment with a similar color, whether they are in powder ( $R^* \geq 75.64\%$ ) or coating form ( $R^* \geq 78.59\%$ ). Moreover, the pigments presented excellent coloring performance when coated on an aluminum sheet substrate and showed good thermal/chemical stability. To sum up, our results suggest that these vanadium doped  $\text{BiPO}_4$  pigments could be used as novel cool color pigments in future. For example, they could be used as roofing materials to reduce heat build-up.

## Conflicts of interest

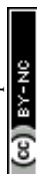
There are no conflicts of interest to declare.

## Acknowledgements

This project was funded by the Priority Academic Program Development of Jiangsu Higher Education Institutions.

## References

- 1 R. Oka and T. Masui, *RSC Adv.*, 2016, **6**, 90952–90957.
- 2 W. Zheng and J. Zou, *RSC Adv.*, 2015, **5**, 87932–87939.
- 3 E. S. Cozza, M. Alloisio, A. Comite, G. Di Tanna and S. Vicini, *Sol. Energy*, 2015, **116**, 108–116.
- 4 R. Levinson, P. Berdahl and H. Akbari, *Sol. Energy Mater. Sol. Cells*, 2005, **89**, 319–349.
- 5 R. Levinson, P. Berdahl and H. Akbari, *Sol. Energy Mater. Sol. Cells*, 2005, **89**, 351–389.
- 6 L. Yuan, X. Weng, M. Zhou, Q. Zhang and L. Deng, *Nanoscale Res. Lett.*, 2017, **12**, 597.
- 7 Y. Shi, M. Zhong, Z. Zhang and D. Wang, *Ceram. Int.*, 2017, **43**, 5979–5983.
- 8 L. Yuan, A. Han, M. Ye, X. Chen, C. Ding and L. Yao, *Ceram. Int.*, 2017, **43**, 16488–16494.
- 9 A. K. V. Raj, P. Prabhakar Rao, S. Sameera and S. Divya, *Dyes Pigm.*, 2015, **122**, 116–125.
- 10 Y. Zhang, Y. Zhang, X. Zhao and Y. Zhang, *Dyes Pigm.*, 2016, **131**, 154–159.
- 11 Z. Wu, R. R. Huang, H. Yu, Y. C. Xie, X. Y. Lv, J. Su, Y. F. Long and Y. X. Wen, *Materials*, 2017, **10**, 134.
- 12 P. Dong, G. Hou, C. Liu, X. Zhang, H. Tian, F. Xu, X. Xi and R. Shao, *Materials*, 2016, **9**, 968.
- 13 Y. Li, Y. Wang, Y. Huang, J. Cao, W. Ho, S. Lee and C. Fan, *RSC Adv.*, 2015, **5**, 99712–99721.
- 14 H. Lv, J. Guang, Y. Liu, H. Tang, P. Zhang, Y. Lu and J. Wang, *RSC Adv.*, 2015, **5**, 100625–100632.
- 15 A. I. Becerro, J. Criado, L. C. Gontard, S. Obregón, A. Fernández, G. Colón and M. Ocaña, *Cryst. Growth Des.*, 2014, **14**, 3319–3326.
- 16 J. Wang, J. Li, H. Li, S. Duan, S. Meng, X. Fu and S. Chen, *Chem. Eng. J.*, 2017, **330**, 433–441.
- 17 J. Zhang, Z. Yu, J. Guo, W. Yan and W. Xue, *J. Alloys Compd.*, 2017, **703**, 156–162.
- 18 X. Shi, Y. Liu, J. Zhang, K. Zhang, J. Li, H. Zuo and P. Li, *Ceram. Int.*, 2015, **41**, 6683–6686.
- 19 M. H. Fulekar, A. Singh, D. P. Dutta, M. Roy, A. Ballal and A. K. Tyagi, *RSC Adv.*, 2014, **4**, 10097–10107.
- 20 J. Cao, B. Xu, H. Lin and S. Chen, *Chem. Eng. J.*, 2013, **228**, 482–488.
- 21 Y. Zhu, Q. Ling, Y. Liu, H. Wang and Y. Zhu, *Appl. Catal., B*, 2016, **187**, 204–211.
- 22 H. Dong, Z. Cao, R. Shao, Y. Xiao, W. He, Y. Gao and J. Liu, *RSC Adv.*, 2015, **5**, 63930–63935.
- 23 R. Yang, A. Han, M. Ye, X. Chen and L. Yuan, *Sol. Energy Mater. Sol. Cells*, 2017, **160**, 307–318.
- 24 ASTM G159-98, American Society for Testing and Materials, West Conshohocken, PA, USA, 1998.
- 25 Y. A. Alsabah, M. S. AlSalhi, A. A. Elbadawi and E. M. Mustafa, *Materials*, 2017, **10**, 469.
- 26 C. I. de l'Eclairage, *Recommendations on Uniform Colour Spaces, Colour Difference Equations, Psychometrics Colour Terms*, Paris: CIE, 1978.
- 27 S. Jose and M. L. Reddy, *Dyes Pigm.*, 2013, **98**, 540–546.



- 28 R. Oka, Y. Shobu, F. Aoyama, T. Tsukimori and T. Masui, *RSC Adv.*, 2017, **7**, 55081–55087.
- 29 T. Tsukimori, Y. Shobu, R. Oka and T. Masui, *RSC Adv.*, 2018, **8**, 9017–9022.
- 30 K. Mokhtari and S. Salem, *RSC Adv.*, 2017, **7**, 29899–29908.
- 31 B. S. Naidu, B. Vishwanadh, V. Sudarsan and R. K. Vatsa, *Dalton Trans.*, 2012, **41**, 3194–3203.
- 32 C. Pan and Y. Zhu, *Catal. Sci. Technol.*, 2015, **5**, 3071–3083.
- 33 S. N. Achary, D. Errandonea, A. Munoz, P. Rodriguez-Hernandez, F. J. Manjon, P. S. Krishna, S. J. Patwe, V. Grover and A. K. Tyagi, *Dalton Trans.*, 2013, **42**, 14999–15015.
- 34 Y. Wang, X. Guan, L. Li and G. Li, *CrystEngComm*, 2012, **14**, 7907–7914.
- 35 Y. Liu, Y. Lv, Y. Zhu, D. Liu, R. Zong and Y. Zhu, *Appl. Catal., B*, 2014, **147**, 851–857.
- 36 R. D. Shannon, *Acta Crystallogr., Sect. A: Cryst. Phys., Diffraction, Theor. Gen. Crystallogr.*, 1976, **32**, 751–767.
- 37 S. Wang, M. Jiang, L. Gao, Z. Ma and F. Wang, *Materials*, 2016, **9**, 55.
- 38 A. Tücks and H. P. Beck, *J. Solid State Chem.*, 2005, **178**, 1145–1156.
- 39 L. Sandhya Kumari, P. Prabhakar Rao, A. Narayana Pillai Radhakrishnan, V. James, S. Sameera and P. Koshy, *Sol. Energy Mater. Sol. Cells*, 2013, **112**, 134–143.
- 40 A. Han, M. Ye, M. Zhao, J. Liao and T. Wu, *Dyes Pigm.*, 2013, **99**, 527–530.
- 41 G. Zeng, J. Yang, R. Hong, Z. Li, Y. Chen, F. Li, Q. Wu, L. Liu and X. Jiang, *Ceram. Int.*, 2018.
- 42 L. Gao, Z. Ma, S. Wang, F. Wang and C. Yang, *Materials*, 2014, **7**, 4982–4993.
- 43 L. Yuan, A. Han, M. Ye, X. Chen, L. Yao and C. Ding, *Dyes Pigm.*, 2018, **148**, 137–146.
- 44 B. Bae, N. Takeuchi, S. Tamura and N. Imanaka, *Dyes Pigm.*, 2017, **147**, 523–528.

